JATIS Journal of Astronomical Telescopes, Instruments, and Systems

RESEARCH PAPER

Broadband chromatic spherical aberration correction in refracting telescopes: a dual-correction strategy combining spherical aberration equalization and an aspheric surface compensation

Jianan Cong,[a,b,c] **Zhihui Yang**,[d,e] **Zhengyang Li**,[a,b,*] **Zhixu Wu**,[f,*] **Jiali Chen**,[a,b,c] **and Kaiwen Zheng**[a,b,c]

[a]Chinese Academy of Sciences, Nanjing Institute of Astronomical Optics and Technology, Nanjing, China
[b]Nanjing Institute of Astronomical Optics and Technology, CAS Key Laboratory of Astronomical Optics and Technology, Nanjing, China
[c]University of Chinese Academy of Sciences, Beijing, China
[d]Nanjing University of Posts and Telecommunications, School of Science, Nanjing, China
[e]Chinese Academy of Sciences, Purple Mountain Observatory, Nanjing, China
[f]Nanchang University, Nanchang, China

ABSTRACT. Traditional apochromatic refracting telescopes only achieve spherical aberration correction at a single wavelength and exhibit significant wavelength-dependent spherical aberration (spherochromatism), which severely constrains their broadband imaging performance in high-precision astrometric applications and wide-field surveys. We propose a dual-correction strategy integrating chromatic aberration equalization and aspheric compensation, achieving diffraction-limited imaging significantly better than the traditional apochromat. Specifically, a 6-in. triplet refractor designed using this method achieves an on-axis Strehl ratio greater than 99% across the spectral range from the *g*-line to the *r*-line, whereas the 6-in. quadruplet refractor achieves an on-axis Strehl ratio greater than 99.95% from the ultraviolet *i*-line to the near-infrared *t*-line. Astrometric accuracy simulation shows that this design enables sub-pixel centroiding (<15 mas) for 16th-magnitude stars. The designs support the application of wide-field (with short focal length) and multiband solar observation and can also eliminate manufacturing error accumulation caused by wavelength mismatch between testing and operational bands in conventional designs.

 [DOI: 10.1117/1.JATIS.11.3.034007]

Keywords: refracting telescopes; apochromat; chromatic spherical aberration; aspheric surfaces; astrometry

Paper 25158G received Jun. 12, 2025; revised Aug. 22, 2025; accepted Sep. 11, 2025; published Sep. 30, 2025.

1 Introduction

In the historical development of telescopes, refracting telescopes have consistently remained a classic category of telescopes, providing distinctive advantages in numerous aspects of astronomy. In the astrometric measurements, the inherent stability of a telescope is critical for achieving high-precision measurements. The angular deviation of the ray induced by reflection is

*Address all correspondence to Zhengyang Li, zyli@niaot.ac.cn; Zhixu Wu, wuzhixu@ncu.edu.cn

2329-4124/2025/$28.00

larger than that of refraction for given surface perturbations in the telescope. Consequently, positional perturbations of reflective surfaces amplify optical errors more significantly than refractive interfaces. Furthermore, the optical path of a refracting telescope with a compact lens arrangement is generally shorter than the reflector telescope system. These characteristics of refractive telescopes significantly enhance the system stability and enable high precision accuracy in astrometric measurements. Therefore, high-precision star catalogs obtained from ground-based observatories, such as the United States Naval Observatory CCD Astrograph Catalogue (UCAC), are still derived from observations made with an 8-in. (20 cm) aperture refracting telescope. For stars in the 10th to 14th magnitude range, the astrometric error is ~15 to 20 mas.[1] Refractive telescopes also exhibit unique advantages in other astronomical fields. For example, because there is no secondary mirror to block the light, refracting telescopes are easier to achieve a higher contrast image, which makes them more suitable for observing the fine structure of the Sun's surface. Although off-axis reflective systems can also avoid the impact of aperture obscuration, the manufacturing and assembly of off-axis aspherical surfaces are extremely challenging. In addition, the off-axis design is not conducive to polarization measurement. The wide-field capability of refractive telescopes enables cost-effective deployment of small-aperture arrays for rapid high-frequency large-area sky surveys.

With the emergence of modern extra-low dispersion materials, it is possible to achieve a refracting telescope that fully corrects for primary chromatic aberration and secondary spectra by balancing chromatic aberration and spherical aberration, which is also named an apochromatic telescope. In an apochromatic telescope, the spherical aberration is under-corrected in the red band and over-corrected in the blue band, and the spherical aberration is lowest in the green band. Spherochromatism, manifested as wavelength-dependent spherical aberration in broadband observations, fundamentally constrains refractive telescope performance in high-precision applications of astronomy. For example, in studying the energy storage process, triggering mechanisms, energy release and transport, radiation, and dynamic evolution of solar eruptions requires high-resolution and high-precision measurements of the brightness field across different layers of the solar atmosphere (photosphere, chromosphere, and lower corona).[2] The solar telescopes are necessary to perform multichannel observations for measuring many characteristic spectral lines, such as the H_α line ($\lambda = 656.3$ nm) and the sodium d line ($\lambda = 589.0$ nm) in the photosphere; the K_α ($\lambda = 393.4$ nm) and K_β ($\lambda = 396.9$ nm) lines of Ca in the chromosphere; and the high-temperature ion spectral lines (e.g., the Fe XI line, $\lambda = 789.2$ nm) of the corona. Each spectral line observation has a very narrow bandwidth, but the lines are distributed over a wide spectral range, requiring the telescope to maintain high resolution across a broad wavelength band. Traditional refracting telescopes with apochromatic objectives have minimal spherical aberration only at one particular wavelength, and the performance declines dramatically at other wavelengths due to the residual spherical aberration, making it difficult to achieve high-precision observations over a wide spectral range covering these critical spectral lines. In another application area of refracting telescopes in fast sky surveys, it is generally desirable to have a telescope with a short focal length to achieve a large field of view. As the spherical aberration is inversely proportional to the third power of the focal length, the performance of a traditional apochromat will deteriorate dramatically due to the sharp increase in chromatic spherical aberration when the focal length decreases.

To enhance the optical performance of refracting telescopes, several different improvement methods currently exist. One approach is to incorporate aspherical surfaces into the system [Fig. 1(b)]. Although aspherical surfaces can modify the spherical aberration of the system, the design still relies on the classical apochromatic design concept, which balances the magnitude of spherical aberration across different wavelengths through chromatic spherical aberration adjustment. The additionally introduced aspherical surfaces cannot eliminate spherical aberration at all wavelengths within the entire spectral range—if the spherical aberration at one end of the spectrum is reduced, the spherical aberration at the other end of the spectrum will increase correspondingly. Therefore, in such cases, aspherical surfaces can only be used to improve spherical aberration at the central wavelength and cannot significantly enhance the telescope's performance over a wide wavelength range. In addition, there are other design methods to improve chromatic spherical aberration. Using wider air gaps, the correction of chromatic spherical aberration can be achieved[3] [Fig. 1(c)]. However, wider air gaps make the lens chamber more prone to

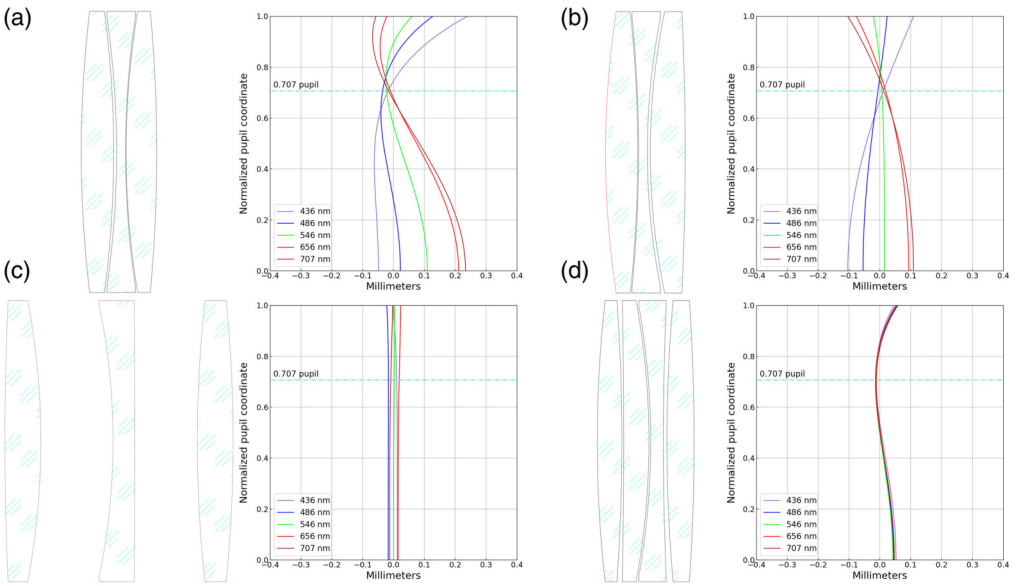

Fig. 1 Several different design methods of refracting telescopes: (a) Traditional apochromatic design; (b) improvement of spherical aberration at the central wavelength by adding aspheric surfaces (the red surface is a quadric asphere); (c) correction of chromatic spherical aberrations through wide air gaps; (d) improvement of chromatic aberration and chromatic spherical aberration correction by increasing the number of lenses.

deformation, undermining the inherent structural advantage of the refractor system in terms of stability. Furthermore, the correction of axial chromatic aberration and chromatic spherical aberration in telescopes can be improved by increasing the number of lenses [Fig. 1(d)]. However, more lenses introduce more air–glass interfaces, which lead to increased stray light, reducing the system's light transmittance efficiency and image contrast. Additional lenses also bring more errors in processing and assembly, making it more challenging to manufacture high-quality objective lenses. Meanwhile, whether it is wider air gaps or more lenses, both will increase the volume and weight of the system as well as the time required for thermal equilibrium.

Different from the design ideas of refracting telescopes mentioned above, this work proposes a dual-correction strategy to correct for chromatic aberration as well as achromatic spherical aberration of the refractive lens. First, through optimization of chromatic aberration, including chromatic spherical aberration, the spherical aberration magnitude is rendered nearly equal across all wavelengths. Second, the spherical aberrations across all the wavelengths are corrected as a whole by incorporating an asphere surface. With this method, the system can obtain an apochromatic refraction system without chromatic spherical aberration. For designing the refracting telescope with a fast focal ratio, although fast focal ratio exhibits greater spherical aberration across all the wavelengths, its near-uniform magnitude across wavelengths and can be easily corrected by modifying the asphericity of the aspheric surface. This design approach has excellent versatility for designing refractive optical systems with different numbers of lenses, such as quadruplet refracting telescopes, which coverage of a very wide wavelength range from ultraviolet to near infrared. This type of refracting telescope designed with our method can achieve a Strehl ratio close to 1 over the entire design spectral range within the paraxial field of view. As the performance of the telescope at this stage is only limited by manufacturing and assembly errors, this article also analyzes the characteristics of this design in the manufacturing process.

2 Design Method

2.1 Dual-Correction Strategy for Correction of Chromatic Spherical Aberration

For traditional apochromatic designs, once the materials have been selected to correct axial chromatic aberration (ensuring that the spherical aberration curves for blue, green, and red

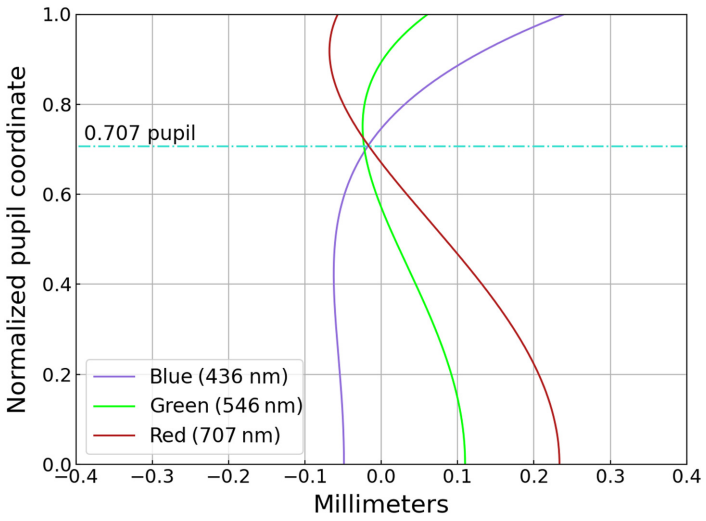

Fig. 2 Spherical aberration curve of traditional apochromat.

wavelengths intersect at the 0.707 normalized pupil position), the next primary design goal is to minimize the spherical aberration across the entire design wavelength range. To achieve this, designers typically allow under-correction of spherical aberration at the red end of the spectrum and over-correction at the blue end, ultimately finding a balanced state that minimizes spherical aberration over a broad wavelength band (Fig. 2). In this balanced state, any further reduction of spherical aberration at one end of the spectrum would lead to an increase at the other end, thus degrading the overall performance of the telescope.

By contrast, we adopted a fundamentally different design philosophy. Our primary design goal is the elimination of spherochromatism, aiming to make the spherical aberration consistent across different wavelengths. As a trade-off for eliminating spherochromatism, the telescope exhibits strong spherical aberration throughout the entire design wavelength range [Fig. 3(a)] —a condition that traditional apochromatic design aims to avoid. However, by introducing an aspheric surface, we are able to eliminate these spherical aberrations and achieve a refractive telescope that is highly corrected for both chromatic and spherical aberrations across the full design spectrum [Fig. 3(b)]. This refractive telescope is nearly aberration-free on-axis, a performance level that traditional apochromatic design methods cannot attain.

This design method possesses excellent universality and is not limited to a specific optical configuration. Figure 4 presents several refracting telescopes designed using this method, each incorporating a different number of lenses. The red surfaces indicate quadratic aspheres. All the telescopes share the same aperture and focal length ($D = 150$ mm, $f' = 1200$ mm), and each

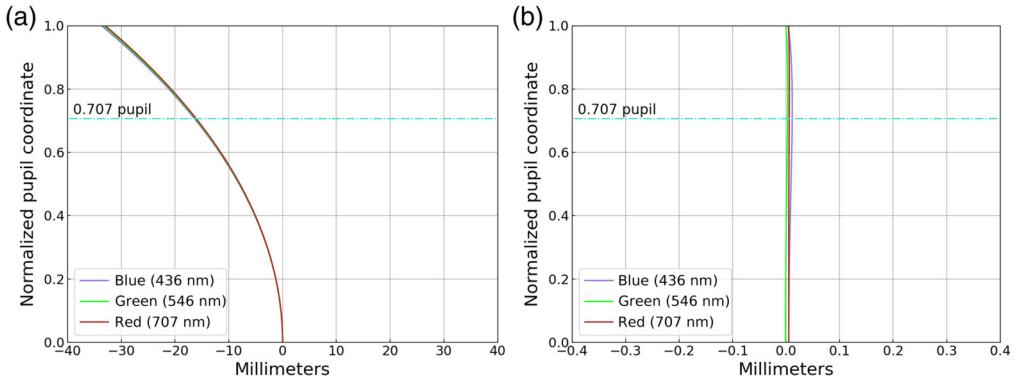

Fig. 3 Dual-correction strategy for correction of chromatic spherical aberration. (a) Eliminating chromatic spherical aberration; (b) introducing an aspheric surface eliminates spherical aberrations.

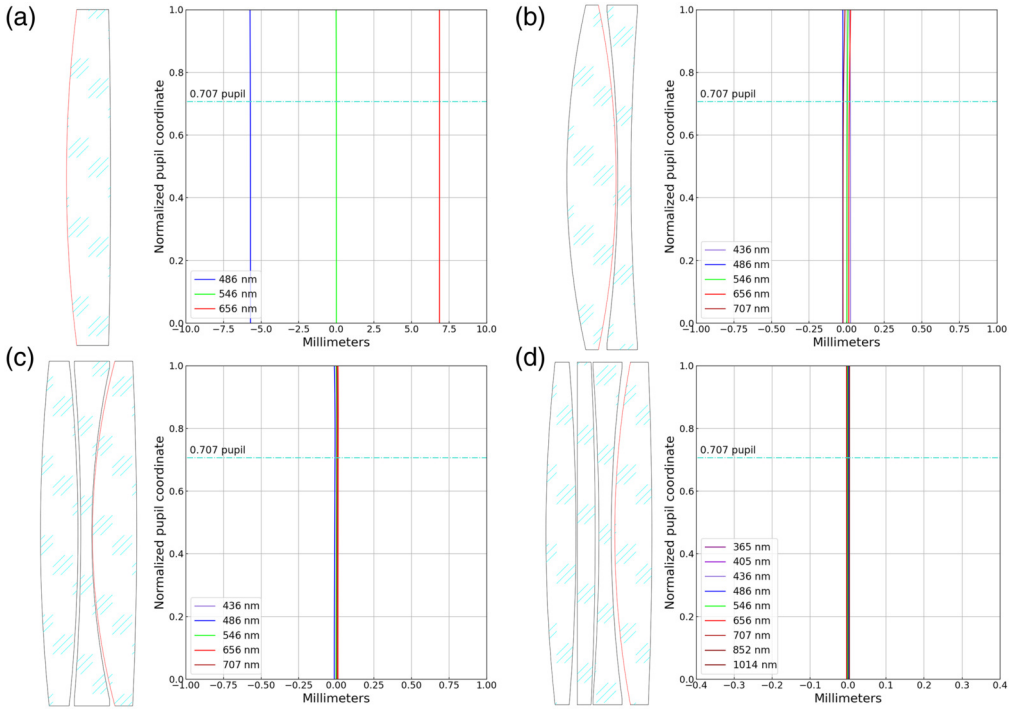

Fig. 4 Designs of chromatic and spherical aberration-corrected refracting telescopes with different numbers of lenses, where the red surfaces are quadric aspheres: (a) singlet, (b) doublet, (c) triplet, and (d) quadruplet.

achieves the elimination of chromatic spherical aberration. The main difference lies in the degree of axial chromatic aberration correction.

The following provides a detailed introduction to this design method using the most representative triplet configuration in apochromatic refracting telescopes as an example. The dispersion properties of optical glass are commonly described by the Abbe number V, which is defined as

$$V = \frac{n_d - 1}{n_F - n_C}. \tag{1}$$

where n_d, n_F, and n_C are the refractive indices of the glass material in the Fraunhofer d ($\lambda = 587.6$ nm), F ($\lambda = 486.1$ nm), and C ($\lambda = 656.3$ nm) lines, respectively. As the sensitivity of modern sensors at the deep blue and deep red ends is much higher compared with film, the design of the apochromatic system using the g ($\lambda = 435.8$ nm), r ($\lambda = 706.5$ nm), and e ($\lambda = 546.1$ nm) lines to calculate the Abbe number

$$V_e = \frac{n_e - 1}{n_g - n_r}. \tag{2}$$

For an apochromatic system consisting of three thin lenses with a focal length of f', the following conditions must be satisfied:

$$\frac{1}{f_1'} + \frac{1}{f_2'} + \frac{1}{f_3'} = \frac{1}{f'}. \tag{3}$$

where f_1', f_2', and f_3' are the focal lengths of the three lenses, respectively. To correct the color difference between blue (g-line) and red (r-line), it should satisfy the equation[4]

$$\frac{1}{f_1' V_{e1}} + \frac{1}{f_2' V_{e2}} + \frac{1}{f_3' V_{e3}} = 0. \tag{4}$$

To correct the secondary spectra so that the green (e-line) has the same focal position as the blue and red, it should satisfy the equation [4]

$$\frac{P_{ge1}}{f_1' V_{e1}} + \frac{P_{ge2}}{f_2' V_{e2}} + \frac{P_{ge3}}{f_3' V_{e3}} = 0. \tag{5}$$

where P_{ge1}, P_{ge2}, and P_{ge3} are the relative dispersion of the three lens glass materials, respectively, and are defined as follows:

$$P_{ge} = \frac{n_g - n_e}{n_g - n_r}. \tag{6}$$

Neglecting the thickness and spacing of the lenses and considering that the entrance pupil coincides with the lens, according to the theory of third-order aberration, the third-order aberration coefficient of the lens group can be expressed as[5]

$$SPHA = \sum_{i=1}^{m} \left\{ \frac{\beta_i}{2} + \frac{n_i^2 \varphi_i^3}{8(n_i - 1)^2} - \frac{n_i \varphi_i}{2(n_i + 2)} \left(\frac{1}{s_i} + \frac{\varphi_i}{2} \right)^2 + \frac{\varphi_i}{2n_i(n_i + 2)} \left[\frac{n_i + 2}{2(n_i - 1)} \sigma_i - 2(n_i + 1) \left(\frac{1}{s_i} + \frac{\varphi_i}{2} \right) \right]^2 \right\}, \tag{7}$$

$$COMA = \sum_{i=1}^{m} \frac{\varphi_i}{2n_i} \left[\frac{n_i + 2}{2(n_i - 1)} \sigma_i - 2(n_i + 1) \left(\frac{1}{s_i} + \frac{\varphi_i}{2} \right) \right], \tag{8}$$

$$ASTI = \sum_{i=1}^{m} \frac{\varphi_i}{2}, \tag{9}$$

$$FCUR = \sum_{i=1}^{m} \left(1 + \frac{1}{2n_i} \right) \varphi_i, \tag{10}$$

$$DIST = 0, \tag{11}$$

where

$$\beta = (n - 1) \left(\frac{k_1}{r_1^3} - \frac{k_2}{r_2^3} \right), \tag{12}$$

$$\varphi = \frac{1}{f'} = (n - 1) \left(\frac{1}{r_1} - \frac{1}{r_2} \right), \tag{13}$$

$$\sigma = (n - 1) \left(\frac{1}{r_1} + \frac{1}{r_2} \right), \tag{14}$$

$$s_i = \begin{cases} -\infty & i = 1 \\ \frac{1}{\sum_j^{i-1} \varphi_j} & i > 1 \end{cases}. \tag{15}$$

β is called the deformation coefficient of the lens, k_1 and k_2 are the conic constants of the two surfaces of the lens, respectively, and for a spherical lens, $\beta = 0$. φ is the optical power of the lens.

As for off-axis aberrations, according to Eqs. (3) and (9), the astigmatism of the system is a constant for a given telescope focal length f'. Moreover, both field curvature and astigmatism can be effectively eliminated by introducing a corrector lens in front of the focal plane (similar to a Ritchey–Chrétien telescope). Therefore, the primary aberration that needs to be corrected is coma. Accordingly, for the traditional triplet apochromatic system, the system should satisfy

$$\begin{cases} \varphi_1 + \varphi_2 + \varphi_3 = \varphi \\ \frac{\varphi_1}{V_{e1}} + \frac{\varphi_2}{V_{e2}} + \frac{\varphi_3}{V_{e3}} = 0 \\ SPHA_g = -SPHA_r \\ COMA_e = 0 \end{cases}. \tag{16}$$

For the triplet chromatic spherical aberration-free system, Eq. (16) becomes

$$\begin{cases} \varphi_1 + \varphi_2 + \varphi_3 = \varphi \\ \frac{\varphi_1}{V_{e1}} + \frac{\varphi_2}{V_{e2}} + \frac{\varphi_3}{V_{e3}} = 0 \\ SPHA_g = SPHA_r \\ COMA_e = 0 \end{cases}. \tag{17}$$

For the spherical surface triplet refraction system, the system contains 6 degrees of freedom ($r_1 \sim r_6$), and both Eqs. (16) and (17) are constrained by four equations, so multiple solutions satisfying the conditions can be found. For the traditional apochromatic system described in Eq. (16), because the spherical aberrations at the g-line and r-line are equal in magnitude but opposite in direction, the spherical aberration at the e-line, with a wavelength that lies between those of the g-line and r-line, will be close to zero. At this point, the system reaches a state of equilibrium. Further reducing the spherical aberration at one end of the spectrum will cause an increase in the spherical aberration at the other end.

For the refraction system described in Eq. (17), the system will exhibit consistent spherical aberration at the g-line, e-line, and r-line, which means the chromatic spherical aberration is eliminated. To achieve this consistency in spherical aberration, however, the system will have relatively large spherical aberration as a trade-off. After determining the values of $r_1 \sim r_6$ that satisfy the conditions, a quadratic asphere (with the conic constant of k) is added to the triplet apochromatic system, along with new constraint conditions

$$SPHA_e = 0. \tag{18}$$

Then, the required aspherical coefficients can be solved. At this time, the system simultaneously completes the correction of primary chromatic aberration, secondary spectra, chromatic spherical aberration, spherical aberration, and coma.

2.2 Influence of Focal Length on Spherical Aberration

Furthermore, the design, for the large field of view needed for fast survey observations in time domain astronomy, is usually achieved with shorter focal lengths, which will not only achieve a large field of view, but also reduce the length and size of the system. However, for traditional apochromatic systems, the short focal length is a very big challenge. For a global surface thin lens system where the entrance pupil coincides with the lens, according to Eq. (7) and Eqs. (12)–(15), we can get

$$\begin{aligned} SPHA = \sum_{i=1}^{m} \Bigg\{ & \frac{n_i^2 \varphi_i^3}{8(n_i-1)^2} - \frac{n_i \varphi_i}{2(n_i+2)} \left(\sum_j^{i-1} \varphi_j + \frac{\varphi_i}{2} \right)^2 \\ & + \frac{\varphi_i}{2n_i(n_i+2)} \left[\frac{n_i+2}{2(n_i-1)} q_i \varphi_i - 2(n_i+1) \left(\sum_j^{i-1} \varphi_j + \frac{\varphi_i}{2} \right) \right]^2 \Bigg\}, \end{aligned} \tag{19}$$

where q is the shape factor of the lens

$$q = \frac{r_2 + r_1}{r_2 - r_1}. \tag{20}$$

When q_i remains constant, according to Eqs. (16) and (17), it can be obtained that the optical power φ_i of the lens is proportional to the total optical power φ of the system, and therefore, it can be set

$$\varphi_i = a_i \varphi, \tag{21}$$

Bringing Eq. (21) into Eq. (19) yields

$$\begin{aligned} SPHA = \varphi^3 \sum_{i=1}^{m} \Bigg\{ & \frac{n_i^2 a_i^3}{8(n_i-1)^2} - \frac{n_i a_i}{2(n_i+2)} \left(\sum_j^{i-1} a_j + \frac{a_i}{2} \right)^2 \\ & + \frac{a_i}{2n_i(n_i+2)} \left[\frac{n_i+2}{2(n_i-1)} q_i a_i - 2(n_i+1) \left(\sum_j^{i-1} a_j + \frac{a_i}{2} \right) \right]^2 \Bigg\}. \end{aligned} \tag{22}$$

According to Eq. (22), the system's spherical aberration is directly proportional to the cube of the system's optical power, that is, inversely proportional to the cube of the system's focal

length f'. Therefore, as the system's focal length decreases, the telescope's spherical aberration increases rapidly. Traditional apochromatic systems exhibit opposite spherical aberrations at the two ends of the design spectral range, making it impossible to correct for spherical aberration. By contrast, the chromatic spherical aberration-free system allows for the correction of increased spherical aberration as the spherical aberrations are similar across the design spectrum, enabling the realization of an optical system with short focal length, compact size, wide field of view, and excellent image quality.

Meanwhile, in addition to spherical aberration, chromatic aberration also varies with the focal length. For a triplet refractor, although it can converge the focal points of three wavelengths (referred to as the g, e, and r lines, respectively, in this paper) to the same point, the focal points of other wavelengths still deviate. Therefore, the concept of "Tertiary Spectrum" can be introduced to measure the chromatic aberration of the system, defined as the separation between the focal points of two additional wavelengths (denoted as a and b, respectively):[6]

$$\text{Tertiary Spectrum} = f'_a - f'_b = \frac{f'}{\delta P_{ge2}(V_{e1} - V_{e3})}[-P_{ab1}(P_{ge3} - P_{ge2}) + P_{ab2}(P_{ge3} - P_{ge1}) - P_{ab3}(P_{ge2} - P_{ge1})], \tag{23}$$

where

$$\delta P_{ge2} = (P_{ge3} - P_{ge1})\frac{V_{e2} - V_{e3}}{V_{e1} - V_{e3}} - (P_{ge3} - P_{ge2}), \tag{24}$$

$$P_{ab} = \frac{n_a - n_e}{n_a - n_b}. \tag{25}$$

Therefore, the chromatic aberration of a telescope is proportional to the focal length of the system, which theoretically applies to both traditional apochromatic designs and new design approaches. However, it should be noted that as the performance of traditional apochromatic systems is mainly limited by chromatic spherical aberration, in practical optimization, to achieve the best system performance, it is sometimes necessary to sacrifice a certain degree of axial chromatic aberration correction to reduce the system's chromatic spherical aberration. This leads to differences in axial chromatic aberration between the two designs. This phenomenon is more pronounced in short-focal-length systems, as demonstrated in the examples in Sec. 3.

3 Triplet Chromatic Spherical Aberration Free Refracting Telescope

3.1 Optical Material Selection for Chromatic Aberration Correction

By solving the system of Eqs. (3)–(5), the optical power distribution of the triplet apochromat, determined by the focal length f and glass materials, can be obtained. In this example, the lenses 1 and 3 are made of the extra-low dispersion material FCD 1. According to Eqs. (4) and (5), it can be found that if the relative dispersion of the paired glass, i.e., lens 2, is the same as that of FCD 1, the solution of the optical power of the lens is not unique, so that more degrees of freedom can be used for the correction of other aberrations. According to Eqs. (3) and (4), if the Abbe number of lens 2 is the same as that of FCD 1, the system of equations has no solution. Therefore the lens 2 should be selected as a material with similar relative dispersion and a large difference in Abbe number with FCD 1. The Abbe number and relative dispersion of Hoya glass materials are illustrated in Fig. 5. The materials that satisfy the conditions are BACD 16 and BACD 5. After testing and comparing, the glass material for Lens 2 is chosen as BACD 16. The parameters of each lens material are shown in Table 1.

3.2 Calculation and Optimization of the Initial Structure

Taking the design of a triplet apochromat for example, this system with a diameter of the entrance pupil $D = 150$ mm and a focal length $f' = 1200$ mm. By adding two extra constraints, a specific initial structure can be derived. The more appropriate constraints for the traditional triplet apochromat are

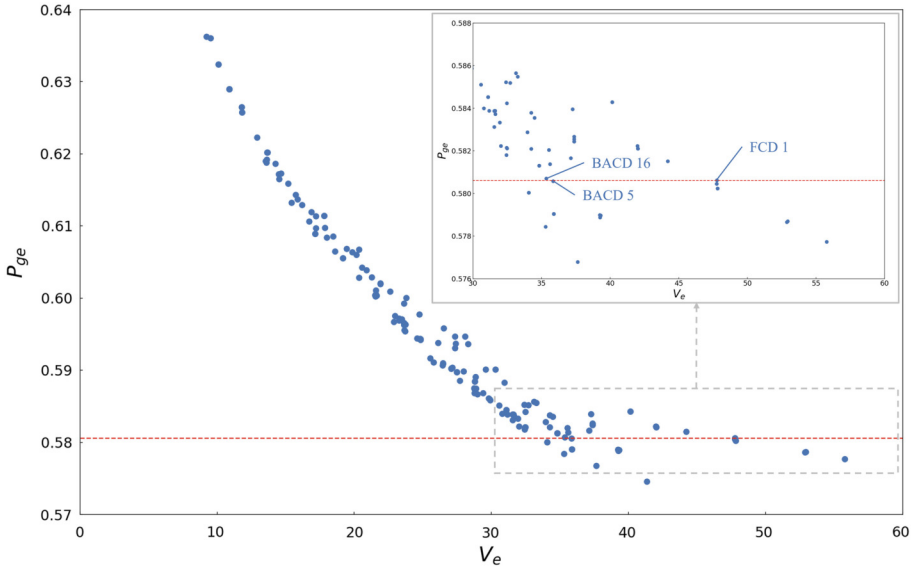

Fig. 5 Abbe number and relative dispersion of Hoya glass materials.

Table 1 Material parameters of triplet refracting telescope.

Parameters	Lens1	Lens2	Lens3
Materials	FCD1	BACD16	FCD1
n_g	1.5045086871	1.6330954664	1.5045086871
n_e	1.4984506252	1.6228623058	1.4984506252
n_r	1.4940750317	1.6154734272	1.4940750317
V_e	47.7733	35.3456	47.7733
P_{ge}	0.5806	0.5807	0.5806

$$\begin{cases} \varphi_1 = \varphi_3 \\ r_3 = -r_4 \end{cases}. \tag{26}$$

In the context of a chromatic spherical aberration-free system, the following constraints are deemed to be more appropriate

$$\begin{cases} \dfrac{\varphi_2\left[(n_{e2}+1)\left(\frac{1}{s_2}+\frac{\varphi_2}{2}\right)\right]^2}{2n_{e2}(n_{e2}+2)} = -\dfrac{\varphi_3\left[(n_{e3}+1)\left(\frac{1}{s_3}+\frac{\varphi_3}{2}\right)\right]^2}{2n_{e3}(n_{e3}+2)} \\ r_1 = -r_2 \end{cases}. \tag{27}$$

The initial structure of the traditional apochromatic system and the chromatic spherical aberration-free system, as obtained from Eqs. (16)–(18), (26), and (27), are shown in Table 2.

The thickness and spacing of the lenses and the higher order aberrations were not considered in the calculation of the above initial structure, and using the ZEMAX optical simulation program, we can further optimize the initial structure.[7]

The optimization merit function mainly consists of five parts: focal length constraint; axial chromatic aberration constraint; spherical aberration and chromatic spherical aberration constraint; coma constraint, and the optimization merit function generated by default in ZEMAX. The first four parts correspond one-to-one with the four constraint equations in Eq. (16). As the change in spherical aberration caused by thickness can be compensated by adjusting the curvature radius of the surface and aspherical coefficients, the aberration that is truly affected by thickness is the lateral chromatic aberration. The optimal glass/air thickness is determined by

Table 2 Initial structure of the triplet refraction systems (A and B represent the traditional apochromatic system and the chromatic spherical aberration-free system, respectively).

Optical element	Radius (mm)		k		f' (mm)	
	A	B	B	Glass	A	B
Lens1	657.80	770.02	0	FCD1	626.27	773.75
	−590.50	−770.02	0			
Lens2	−525.60	−518.12	0	BACD16	−421.77	−421.77
	525.60	533.31	0			
Lens3	492.58	465.79	−0.187	FCD1	626.12	525.87
	−845.12	−594.33	0			

minimizing the lateral chromatic aberration. For the selection of aspherical surfaces, according to the third-order aberration theory Eq. (7), aspherical ization of any surface can achieve spherical aberration correction. In practical design, considering the influence of thickness and off-axis aberrations, there exists an aspherical surface with the best correction effect. The position of

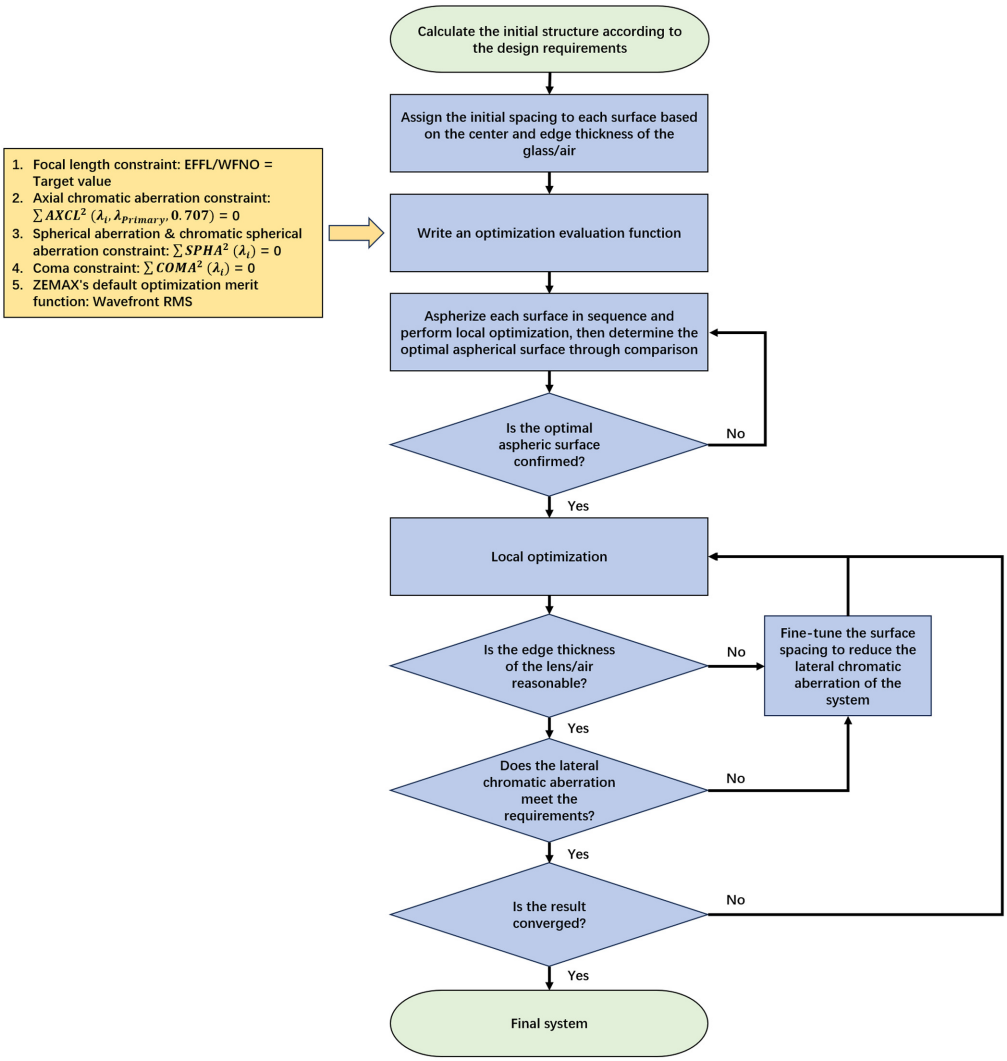

Fig. 6 Optimization flowchart.

Table 3 Parameters of the triplet refraction systems (A and B represent the traditional apochromatic system and the chromatic spherical aberration-free system, respectively).

Optical element	Radius (mm)		k	Thickness (mm)			f' (mm)	
	A	B	B	A	B	Glass	A	B
Lens1	657.80	769.30	0	18.0	17.0	FCD1	627.34	774.79
	−590.60	−769.80	0	1.6	1.3			
Lens2	−523.30	−959.60	0	5.0	5.0	BACD16	−417.33	−415.52
	518.40	355.10	0	0.3	0.3			
Lens3	480.50	302.80	−0.456	17.0	20.0	FCD1	618.48	516.27
	−850.00	−1676.20	0	1181.5	1178.5			

this surface varies with different structures (Fig. 4) and needs to be selected through trials and comparisons during the design process. The process of selecting the optimal aspherical surface can also be simplified by using ZEMAX's function for finding the best aspherical surface. For systems with a longer focal length, sufficient spherical aberration correction can be achieved using a quadric asphere; for systems with a shorter focal length, high-order terms can be appropriately added to improve the correction of high-order spherical aberrations.

The specific optimization process is shown in Fig. 6. The optimized system structures of the two systems are shown in Table 3. In addition, the layouts are shown in Fig. 7. Compared with the traditional design, the new design remains essentially the same in terms of volume and weight, whereas its optical performance has been significantly improved—at the cost of only aspherizing one surface.

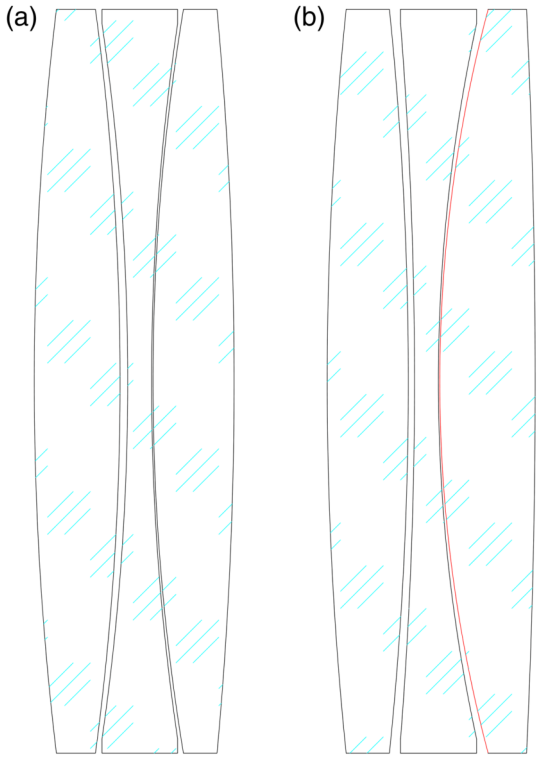

Fig. 7 Optical layouts of two types of triplet refractors. (a) Traditional apochromat; (b) chromatic spherical aberration-free system (the red surface is a quadric asphere).

3.3 Optical Performance

Figure 8 illustrates the optical performance of the two apochromatic systems. In the wavelength range from *g*-line to *r*-line, the maximum axial chromatic aberrations of the two designs are 26.7 μm and 22.2 μm, respectively [Figs. 8(c) and 8(d)]. It can be observed that there is no significant difference in primary chromatic aberration between the two, with the main difference being the correction of spherical aberration. The traditional apochromat retains a certain amount of spherical aberration across all wavelengths [Figs. 8(a) and 8(e)], even in the best-corrected green band. By contrast, the chromatic spherical aberration-free system shows excellent spherical aberration correction across all wavelengths [Figs. 8(b) and 8(f)]. The telescope performs significantly better than the traditional apochromat, especially at the blue-violet and deep red ends of the spectrum, with a Strehl ratio exceeding 99% across the entire range from the *g*-line to the *r*-line [Fig. 8(g)].

The performance advantages described above make the chromatic spherical aberration-free system more suitable for both daytime and nighttime astronomical observations compared with the traditional apochromat. Furthermore, although the triplet refraction system generates significant chromatic aberration in the infrared and ultraviolet regions, this is not a problem for solar observations, which typically focus on narrowband spectra of specific lines. In this case, axial chromatic aberration is not a concern. The chromatic spherical aberration-free system maintains

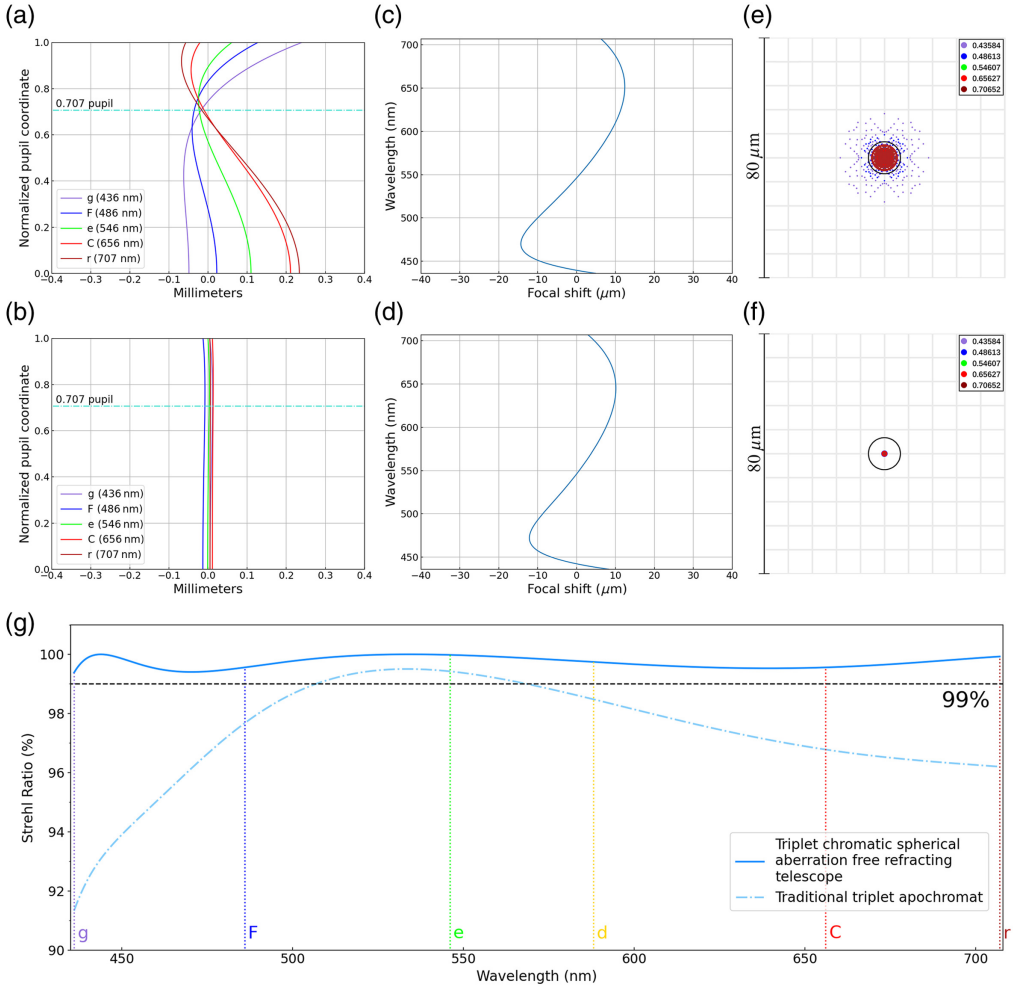

Fig. 8 Optical performance of the two triplet refraction systems in the *g*-line to *r*-line spectral range. The first and second rows represent the traditional apochromatic system and the chromatic spherical aberration-free system, respectively. (a)–(b) Spherical aberration curves; (c)–(d) primary chromatic aberration curves; (e)–(f) axial field point array plots (black circles represent airy disk diameters at the *e*-line.); (g) Strehl ratio curve (at the focal point of the *e*-line).

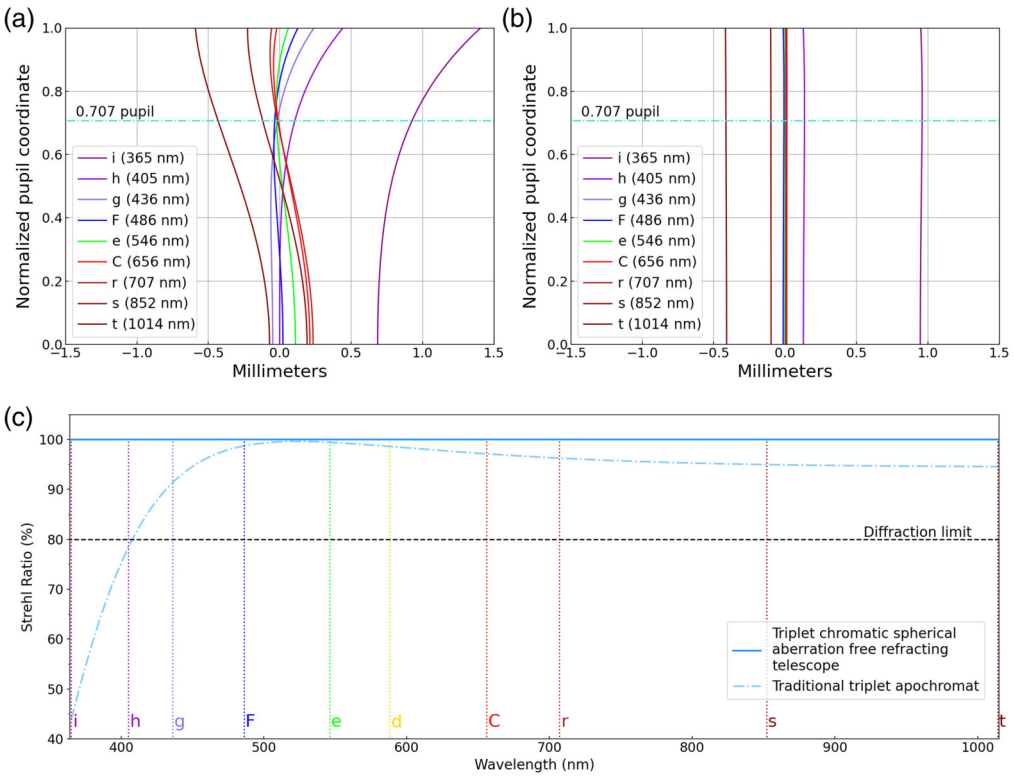

Fig. 9 Optical performance of the two triplet refraction systems in the *i*-line to *t*-line spectral range. (a)–(b) Spherical aberration curves. Left: traditional apochromat, right: chromatic spherical aberration-free system. (c) Strehl ratio curve (at the focal point of each monochromatic wavelength).

spherical aberration correction for ultraviolet and near-infrared spectral lines [Fig. 9(b)], thus providing good image quality even under quasi-monochromatic light. By contrast, the traditional triplet apochromatic system exhibits significant spherical aberration in the ultraviolet and near-infrared spectral lines [Fig. 9(a)], leading to a rapid decrease in Strehl ratio at shorter ultraviolet wavelengths [Fig. 9(c)]. Taking the above model as an example, the traditional apochromat falls below the diffraction limit standard (80% Strehl ratio) at the *h*-line. Therefore, the traditional triplet apochromatic system is not suitable for ultraviolet solar observations.

For the short focal length system, Fig. 10 shows examples of the two triplet refraction systems, with an entrance pupil diameter of $D = 150$ mm and a system focal length $f' = 900$ mm. For the chromatic spherical aberration free system, a fourth-order asphere were used to fully correct the spherical aberration. Compared with the system with $f' = 1200$ mm, the performance of the traditional apochromat significantly deteriorates, with the Strehl ratio at the *g*-line dropping from 91.3% to 58.5%, and at the *r*-line from 96.2% to 76.0%, both falling below the diffraction limit. By contrast, the chromatic spherical aberration-free system correction maintains a Strehl ratio above 99% across the *g*-line to *r*-line range.

In the wavelength range from *g*-line to *r*-line, the maximum axial chromatic aberrations of the two designs are 30.4 and 15.3 μm, respectively [Figs. 10(c) and 10(d)]. Compared with the $F/8$ case [Figs. 8(c) and 8(d)], the variation of axial chromatic aberration with focal length in the chromatic spherical aberration-free system basically follows Eq. (23). However, the traditional apochromatic design exhibits pronounced deviations as the reduction in focal length leads to a substantial increase in spherochromatism, thereby imposing further constraints on its overall performance. To optimize the system performance, the traditional apochromat has to compromise part of the axial chromatic aberration to reduce spherochromatism. The smaller the focal length, the more pronounced the differences in axial chromatic aberration and spherochromatism between the two designs become.

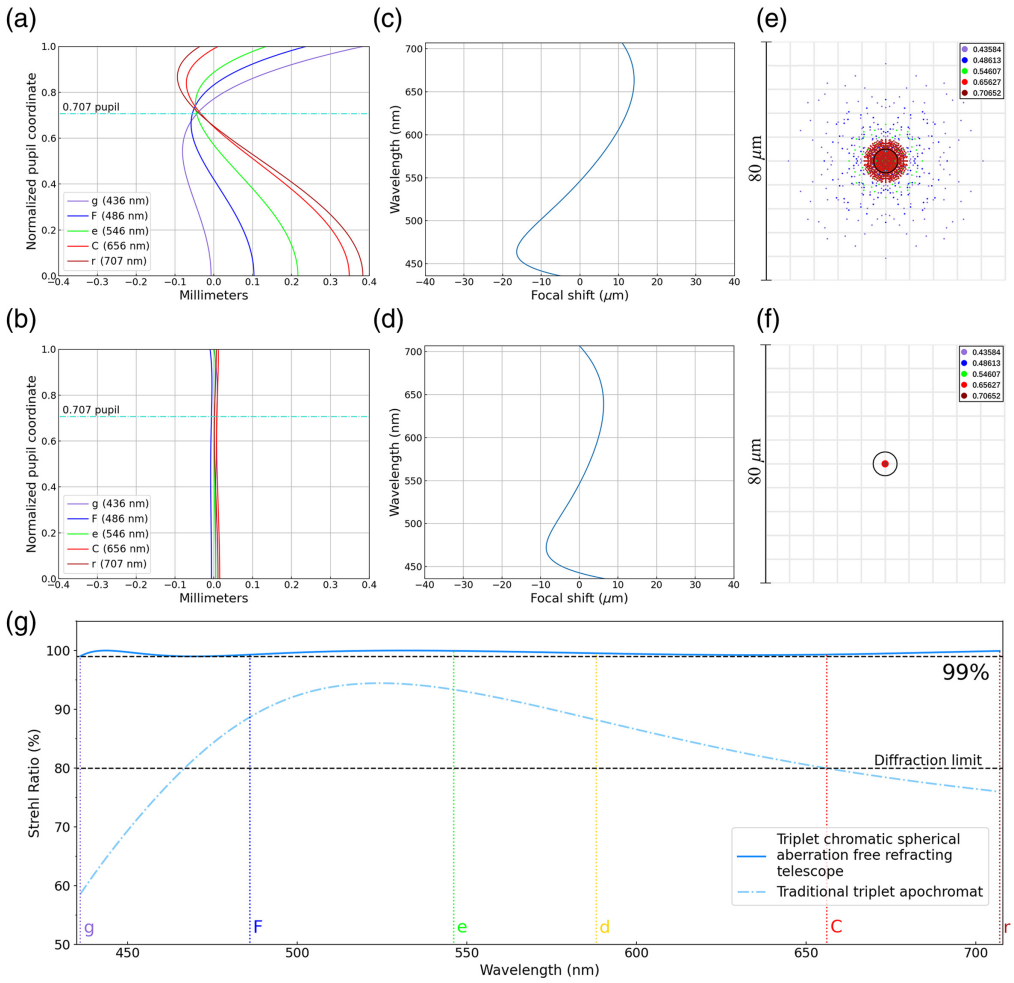

Fig. 10 Optical performance of the two short focal length triplet refraction systems in the *g*-line to *r*-line spectral range at $f' = 900$ mm. The first and second rows represent the traditional apochromatic system and the chromatic spherical aberration-free system, respectively. (a)–(b) Spherical aberration curves; (c)–(d) primary chromatic aberration curves; (e)–(f) axial field point array plots (black circles represent Airy disk diameters at the *e*-line); (g) Strehl ratio curve (at the focal point of the *e*-line).

4 Quadruplet Wide-Band Chromatic Spherical Aberration Free Refracting Telescope

By extending the design approach of the traditional triplet apochromatic system to a quadruplet configuration, a system that corrects both chromatic and spherical aberrations across the ultraviolet to near-infrared spectrum can be achieved [Fig. 4(d)]. This system fully covers the sensitivity range of modern silicon-based CCD/CMOS sensors.[8] Compared with the triplet configuration, the chromatic aberration is further corrected over a broader spectral range. Therefore, it is more advantageous for broadband imaging in nighttime astronomy. It also matches well with optical photometric systems commonly used in modern astronomy, such as the SDSS $u'g'r'i'z'$ system [Fig. 11(d)].[9,10] This cannot be achieved with a triplet refraction system. Such a wideband chromatic spherical aberration-free system is highly suitable for photometric and astrometric telescopes.

For the quadruplet wideband achromatic spherical aberration correction system, the initial design is based on the triplet configuration, with an additional lens introduced to extend the axial chromatic aberration correction range of the telescope. As the number of possible material combinations in a quadruplet is significantly greater than in a triplet, manually determining the optimal material match becomes more challenging. In practice, the best glass material combination is

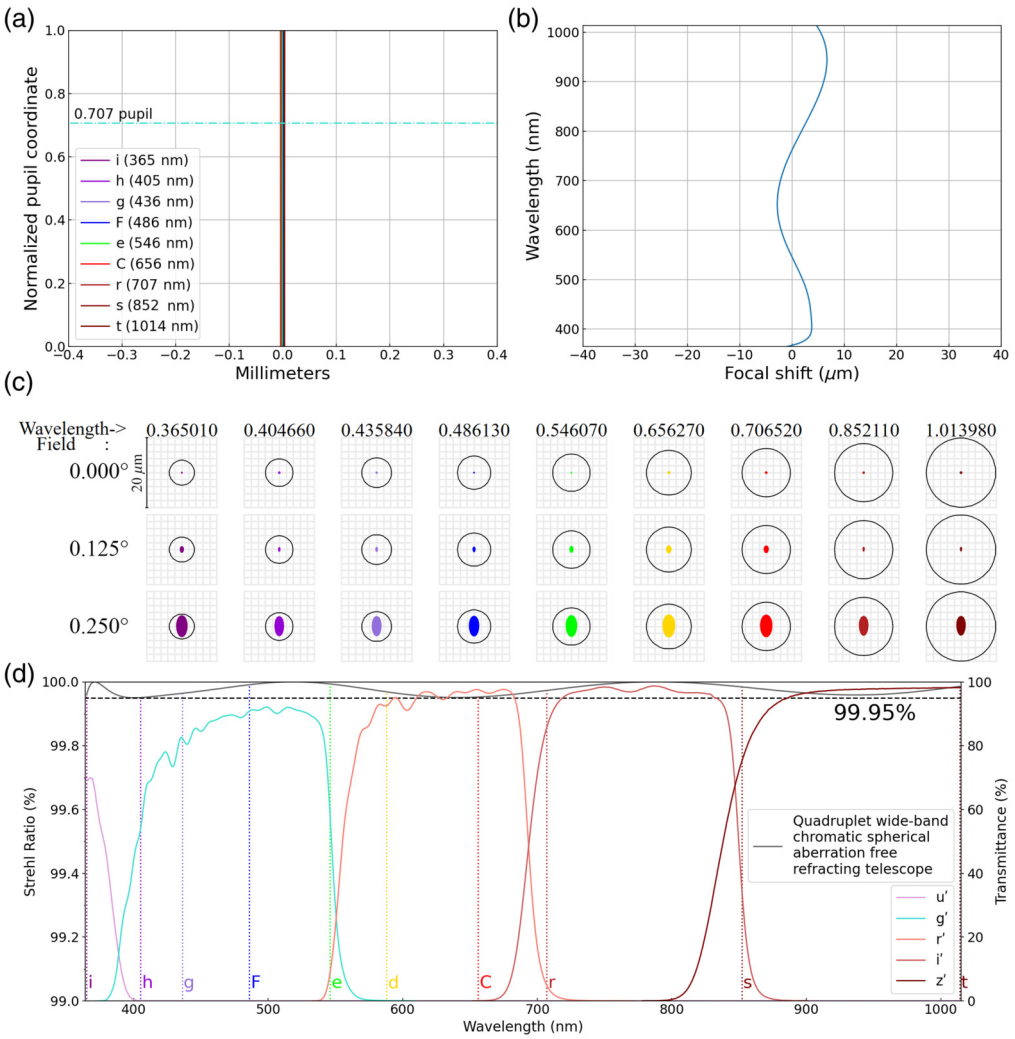

Fig. 11 Optical performance of the wide-band chromatic spherical aberration-free refraction system in the *i*-line to *t*-line spectral range. (a) Spherical aberration curve; (b) primary chromatic aberration curve; (c) point array plots (black circles represent the Airy disk diameters for the corresponding wavelengths); (d) Strehl ratio curve (at the focal point of the e-line, with the colored curves showing the transmission rates of each channel of the $u'g'r'i'z'$ filter system).

identified using the local optimization algorithm in ZEMAX, whereas the optimization procedure and evaluation function still follow those shown in Fig. 6.

Table 4 shows an example with an incident pupil aperture of $D = 150$ mm and $f' = 1200$ mm. The telescope has an axial chromatic aberration of only 9.3 μm from *i*-line to *t*-line [Fig. 11(b)], which is less than $\pm 0.0004\%$ of its own focal length. The on-axis Strehl ratio over the entire range of corrected bands is better than 99.95% [Fig. 11(d)]. Coma aberration is similarly eliminated. The performance is very similar to that of the RC system, with the difference being the absence of the negative effects caused by aperture obstruction.

5 Astrometric Accuracy Simulation

To conduct a more detailed analysis of the advantages of the refractive telescope designed by this method in astrometric applications, we use the PhoSim program for simulation and validation. PhoSim is a set of extremely fast photon Monte Carlo codes that calculate the ab initio physics of the atmosphere and a telescope and camera to simulate realistic optical/UV/IR/X-ray astronomical images. PhoSim does this using modern numerical techniques applied to the physical response of photons (and electrons) to comprehensive physical descriptions of the atmosphere, telescope, and camera. After these detailed physics calculations, PhoSim simply generates

Table 4 Parameters of the quadruplet wide-band chromatic spherical aberration-free refracting telescope.

Optical element	Radius (mm)	k	Thickness (mm)	Glass	f' (mm)
Lens1	726.74	0	13.6	FCD100	955.19
	−980.89	0	0.6		
Lens2	Infinity	0	8.1	F5	2641.20
	−1603.69	0	1.7		
Lens3	−1052.72	0	5.6	S-LAH97	−489.90
	−575.56	0	1.6		
Lens4	425.76	−0.733	16.8	FCD1B	694.86
	−1834.77	0	1176.0		

images by collecting electrons into pixels. The photon/electron interaction physics includes the appropriate application of novel advanced raytracing, diffraction, and quantum mechanical interactions.[11]

The following sections introduce the simulation environment and instrument settings. The observation site is set at Lenghu, Qinghai, China, with specific geographic coordinates of 38.88° N latitude, 93.00°E longitude, and an altitude of 4176.00 m. The observation time, corresponding celestial phenomena, and meteorological conditions (excluding atmospheric turbulence) are listed in Table 5. Regarding the atmospheric turbulence settings, as the selected observation site is the same as that of WFST, the atmospheric turbulence parameters are referenced from the WFST model included in PhoSim. Where the mean outer scale of the turbulent free atmosphere is 38 m, the median outer scale of the turbulent free atmosphere is 32 m, the mean dome seeing is 0.05 arcsec, and the median dome seeing is 0.05 arcsec. PhoSim divides the atmosphere into seven layers,[12] with turbulence settings for each layer detailed in Table 6.

Regarding the instrument settings, the telescope uses g', r', i', and z' filters, with the transmission curve for each channel referenced in Fig. 11(d). The telescope camera parameters are set

Table 5 Observation environment (excluding atmospheric turbulence).

Parameter of the observation environment	Value
Modified Julian day/days	60909.75
Right ascension of moon/degree	146.85
Declination of moon/degree	15.66
Altitude of moon/degree	−35.02
Moon phase/%	0.32
Right ascension of sun/degree	151.99
Declination of sun/degree	11.51
Altitude of sun/degree	−39.57
Ambient temperature/°C	20.0
Relative humidity/%	0
Ambient pressure/mmHg	620.2

Table 6 Atmospheric turbulence parameters at different altitudes.

Number of layers	Low range altitude (m)	Mean altitude (m)	High range altitude (m)	Low range Cn2	Median Cn2	High range Cn2	Log variance of Cn2	Low range Cn2 for ground layer	Median Cn2 for ground layer	High range Cn2 for ground layer	Log variance of Cn2
1	0	2680	2920	0	0	0	0	2.2	2.7	3.3	0.3
2	2920	3160	3410	0.2	0.4	0.7	0.86	0	0	0	0
3	3140	3660	4160	0.03	0.1	0.2	1.16	0	0	0	0
4	4160	4660	5660	0.02	0.1	0.4	1.99	0	0	0	0
5	5660	6660	8660	0.2	0.4	0.6	0.7	0	0	0	0
6	8660	10660	14660	0.15	0.2	0.3	0.56	0	0	0	0
7	14660	18660	22660	0.25	0.3	0.3	0.07	0	0	0	0

according to the specifications of the IMX455 sensor. As the simulation focuses on a single star, the camera resolution is set to 256×256 pixels to reduce computational load. The specific camera parameters are listed in Table 7.[13,14]

The observation target is a single star, which is set to have a flat spectral energy distribution to simplify the simulation. The star's azimuth is set to 0 deg, with an altitude angle of 89 deg, positioned at the center of the telescope's field of view. As the telescope is pointed near the zenith, atmospheric dispersion effects are also ignored. The cloud cover is set to 0, and tolerance effects are neglected. All other physical effects follow the default settings of the program.

The star's AB magnitudes are set to 12, 14, and 16. The telescope's single exposure time is set to 30 s. To reduce the impact of random errors in the simulation, 10 images are taken for each filter channel, and the image sequences are averaged to obtain the final result. Figure 12 presents the imaging results of stars with different magnitudes for the traditional triplet apochromat (corresponding to the optical design in Table 3) and the wide-band chromatic spherical aberration-free refracting telescope (corresponding to the optical design in Table 4) across different channels. In each image, the first row represents the imaging results of the traditional triplet

Table 7 Camera parameter setting.

Parameter of the camera	Value
Pixel size/μm	3.76
Number of x pixels	256
Number of y pixels	256
Sensor material	Silicon
Photosensitive layer thickness/μm	10.0
Full well depth/e–	51000
Nominal temperature/°C	–10.0
Gain of amplifier/e– ADU^{-1}	0.8
Bias value of amplifier	100
Read noise average value/e–	3.48
Dark current/e– pixel^{-1} s^{-1}	0.011
Number of bits in the readout A/D conversion	16

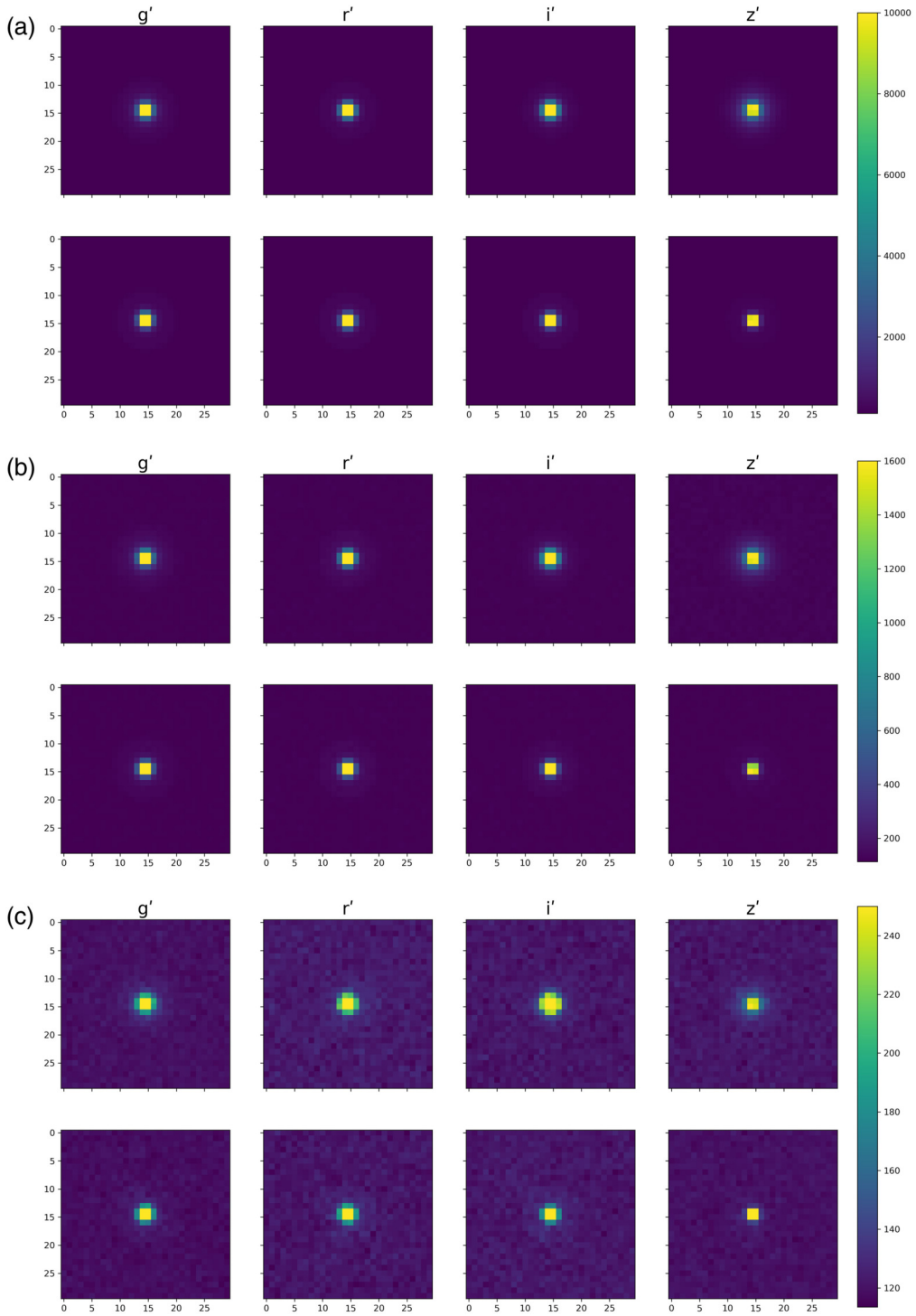

Fig. 12 Imaging of the traditional apochromat and the wide-band chromatic spherical aberration-free refracting telescope across different channels for stars of different magnitudes: (a) 12th magnitude, (b) 14th magnitude, and (c) 16th magnitude.

apochromat, whereas the second row corresponds to the wide-band chromatic spherical aberration-free refracting telescope. A focus compensation of accuracy of 5 μm was applied to both telescopes for each channel to achieve optimal focus. To enhance the visibility of the star profiles, the images of stars with the same magnitude were stretched identically in Fig. 12. Pixel brightness values below or above the corresponding thresholds were truncated, and each image was cropped to retain only the central region.

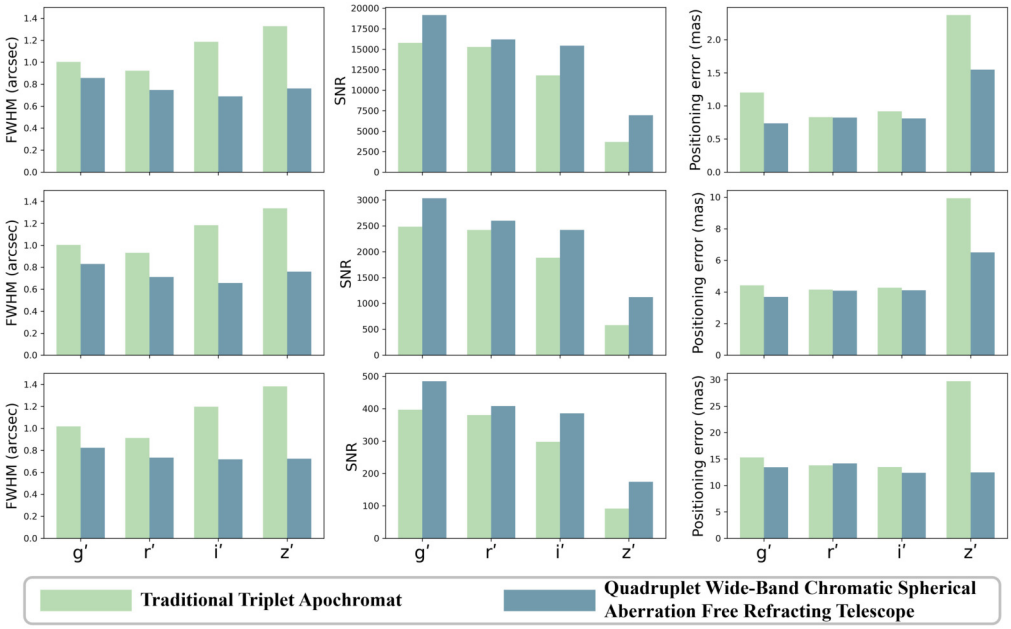

Fig. 13 Statistical data of the simulated star image's FWHM, SNR, and positioning error. The first row corresponds to images of 12th magnitude stars, the second row to 14th magnitude stars, and the third row to 16th magnitude stars.

According to the empirical formula for astrometric positional accuracy, the precision of determining the centroid position of a star is related to the image's signal-to-noise ratio (SNR)[15]

$$\sigma_{meas} = \frac{1}{\pi}\frac{\lambda}{D}\frac{1}{SNR}. \tag{28}$$

According to empirical formulas, under otherwise identical conditions, a higher SNR generally leads to higher measurement accuracy. In the simulation, the star target is artificially placed at the center of the field of view, allowing the actual calculation of the position deviation between the centroid of the simulated star image and the image center, thereby obtaining the positioning error of the simulated star image. Figure 13 presents the statistical data of the full width at half maximum (FWHM), SNR, and positioning error for the simulated star images.

It can be seen that the wide-band chromatic spherical aberration-free refracting telescope generally outperforms the traditional triplet apochromat in terms of FWHM, SNR, and positioning accuracy, especially in the longer-wavelength i' and z' bands. This is particularly important for astrometry as longer-wavelength light is less affected by atmospheric turbulence and is more suitable for astrometric observations.

According to the simulation results, both designs show significantly lower SNR in the z' band compared with other bands, resulting in relatively lower positioning accuracy in this band. This is mainly due to the low quantum efficiency of the silicon-based sensor used in the simulation in the z' band. This issue can be addressed using near-infrared sensors such as InGaAs detectors.

6 Processing and Assembly Errors

In addition to better performance in design, chromatic spherical aberration-free systems also offer advantages in practical fabrication and testing. Laser interferometry is the most commonly used method in optical testing. The traditional apochromatic system minimizes spherical aberration only at a specific wavelength (usually green light), whereas the most commonly used light source for laser interferometers is the helium-neon laser, which emits red light at a wavelength of 632.8 nm. As a result, the telescope detects some degree of spherical aberration. To minimize

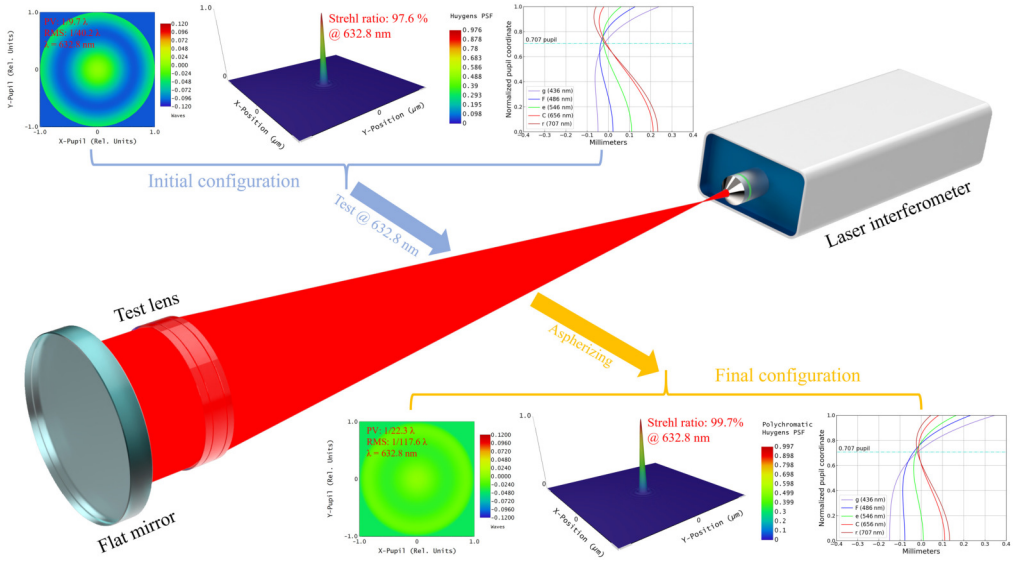

Fig. 14 Mismatch between the wavelength of the light used for testing and the chromatic spherical aberration correction wavelength in the system, leading to deviations between the fabricated optical system and the design (using the traditional triplet apochromat with $f' = 1200$ mm from Sec. 3 as an example).

the detected wavefront aberration, adjustments need to be made to the lens, such as introducing an aspherical surface on one of its surfaces, which would lead to under-correction at the blue wavelength (Fig. 14, using the traditional triplet apochromat with $f' = 1200$ mm from Sec. 3 as an example). In other words, an optical system with chromatic spherical aberration will result in a mismatch between design and testing if the wavelength used in the test differs from the wavelength at which the spherical aberration was corrected in the design. This mismatch can lead to degradation of the actual performance of the fabricated optical system and impose significant limitations.

For chromatic spherical aberration-free systems, spherical aberration is well corrected within the design spectral range. Therefore, as long as the wavelength of the light used for testing is within the design spectral range, the system will perform as expected. Figure 15 illustrates the performance difference between the traditional triplet apochromat and the triplet chromatic spherical aberration-free system, using the $f' = 1200$ mm systems from Sec. 3 as an example. When a 632.8 nm laser is used as the testing light source, the performance difference is shown after minimizing the detected spherical aberration by adjusting the asphericity of the fifth surface. The Strehl ratio of the traditional apochromat in the blue spectral range shows a significant decrease compared with the design value, dropping below the diffraction limit at the g-line. By contrast, the Strehl ratio of the chromatic spherical aberration-free system remains nearly the same as the design value.

We also compared the assembly tolerance sensitivities of several visible-band apochromatic designs presented in Figs. 1 and 8. For each lens, the decenter and tilt tolerances were set to ± 0.05 mm and ± 1 arcmin, respectively, with an inter-lens spacing tolerance of ± 0.03 mm. Within the above tolerance ranges, 500 sets of tolerance combinations were generated in ZEMAX using Monte Carlo random sampling, and the image quality (the 80% encircled energy diameter for $g - r$ polychromatic light) of the 500 perturbed optical systems was calculated. The results (Fig. 16) show that the triplet designs exhibit comparable tolerance margins, with differences between them falling within the simulation's margin of error. By contrast, the quadruplet design, having more lenses, introduces more assembly errors, resulting in significantly lower tolerance margins than the triplet designs. It should be noted that for each design, assembly errors can be compensated during alignment—for example, by adjusting the tilt and decenter of the first lens—thereby significantly improving the final optical performance.

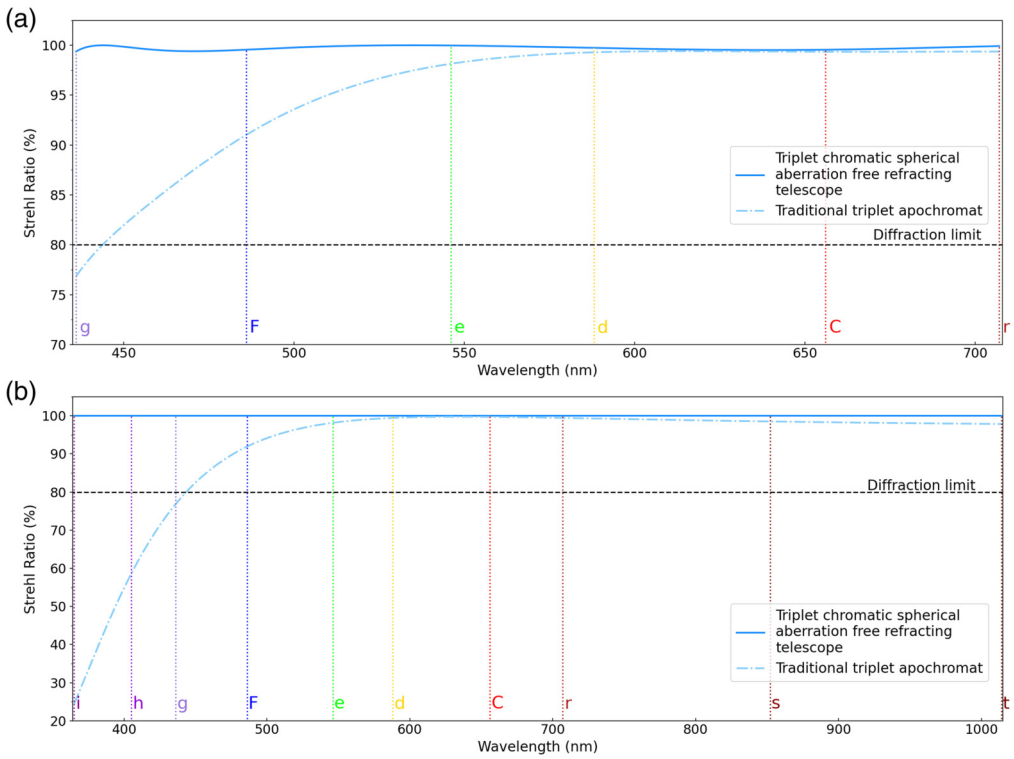

Fig. 15 Strehl ratio curves after testing and fabrication for two triplet refraction systems. (a) At the focal point of the *e*-line; (b) at the focal points of the respective monochromatic wavelengths.

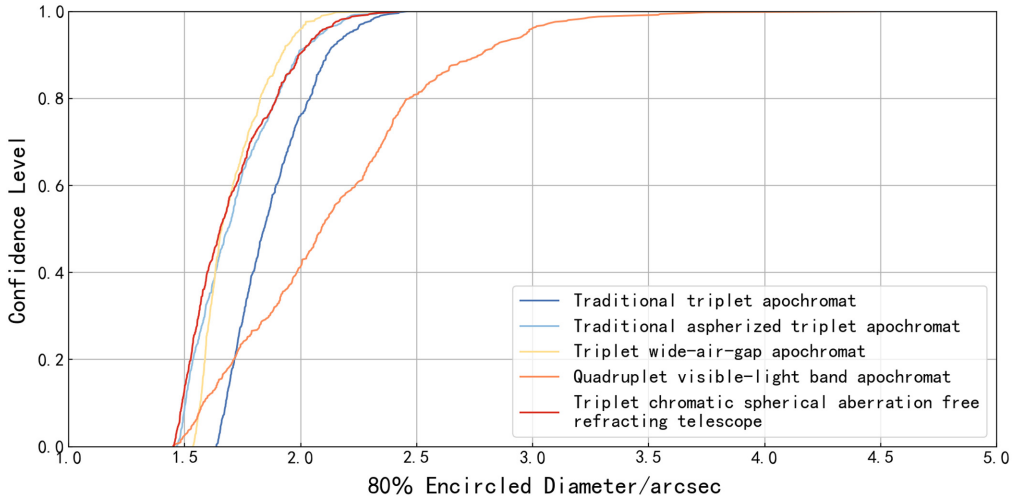

Fig. 16 Statistical results of image quality for several designs under 500 sets of tolerance samples.

7 Conclusion

This study introduces a dual-correction strategy integrating chromatic aberration equalization and aspheric surface compensation, achieving unprecedented broadband chromatic spherical aberration correction in refracting telescopes. Specifically, the proposed design realizes diffraction-limited performance (Strehl ratio >99.95%) across the ultraviolet-to-near-infrared spectrum (365 to 1014 nm) and maintains sub-pixel centroiding accuracy (<15 mas) for stars down to 16th magnitude in diverse spectral bands (e.g., SDSS $u'g'r'i'z'$). The approach further enables compact wide-field systems. Notably, the design avoids aperture obstruction, enhances

image resolution for solar observations, and has good compatibility with test light sources of different wavelengths in optical testing. These advancements position the system as a transformative solution for high-precision astrometry, wide-field surveys, and future space telescopes requiring high-contrast imaging capabilities.

Future work will mainly focus on reducing the impact of errors existing in optical materials, as well as in the processing and assembly processes, on the performance of the final telescope system. A compact refracting telescope ($D = 203$ mm, $F/8$) based on this methodology has entered the engineering verification phase, expected to advance precision accuracy in astrometric measurements. The established spherochromatism correction model extends applicability to space telescopes, providing a theoretical foundation for high-contrast optical systems in exoplanet direct imaging.

Disclosures

The authors declare that there are no financial interests, commercial affiliations, or other potential conflicts of interest that could have influenced the objectivity of this research or the writing of this paper.

Code and Data Availability

Data underlying the results presented in this paper are not publicly available at this time but may be obtained from the authors upon reasonable request.

Acknowledgments

This work was supported by the National Natural Science Foundation of China (Grant No. 12173062). Optical simulated by Zemax Software (Grant No. L119064).

References

1. N. Zacharias et al., "The fourth US Naval Observatory CCD astrograph catalog (UCAC4)," *Astron. J.* **145**, 44 (2013).
2. C. Fang et al., "2.5 m wide-field and high-resolution telescope," *Scientia Sin. Phys. Mech. Astron.* **49**(5), 059603 (2019).
3. W. Smith, *Modern Lens Design*, McGraw-hill (2004).
4. D. Malacara-hernández and Z. Malacara-Hernández, *Handbook of Optical Design*, 3rd ed., CRC Press (2013).
5. M. Born, E. Wolf, and A. Bhatia, *Principles of Optics*, Cambridge University Press (2019).
6. A. Conrady, *Applied Optics and Optical Design, Part One*, Dover Publications (2013).
7. Zemax, "Zemax opticstudio," https://www.zemax.com/ (2013).
8. G. Held, *Introduction to Light Emitting Diode Technology and Applications*, CRC Press (2016).
9. J. A. Smith et al., "The Ugriz standard-star system," *Astron. J.* **123**, 2121 (2002).
10. SDSS Japan Participation Group, "The u'g'r'i'z' standard star system: USNO40 filters," https://www-star.fnal.gov/ugriz/Filters/response.html (accessed 18 April 2025).
11. J. R. Peterson et al., "Simulation of astronomical images from optical survey telescopes using a comprehensive photon Monte Carlo approach," *Astrophys. J. Suppl. Ser.* **218**, 14 (2015).
12. J. R. Peterson et al., "Self-consistent atmosphere representation and interaction in photon Monte Carlo simulations," *Astrophys. J.* **964**, 124 (2024).
13. J. R. Peterson et al., "Sensor distortion effects in photon Monte Carlo simulations," *Astrophys. J.* **889**, 182 (2020).
14. M. R. Alarcon et al., "Scientific CMOS sensors in astronomy: Imx455 and imx411," *Publ. Astron. Soc. Pac.* **135**, 055001 (2023).
15. W. F. Van Altena, *Astrometry for Astrophysics: Methods, Models, and Applications*, Cambridge University Press (2013).

Jianan Cong is a master's student at the Nanjing Institute of Astronomical Optics & Technology, Chinese Academy of Sciences. His main research interests include optical design, active optics, and the study of optical systems under extreme environments.

Biographies of the other authors are not available.